



# Phase heritage during replacement reactions in Ti-bearing minerals

Mark Pearce<sup>1</sup> · Angela Escolme<sup>2</sup>

Received: 10 July 2020 / Accepted: 25 January 2021 / Published online: 4 March 2021  
© The Author(s), under exclusive licence to Springer-Verlag GmbH, DE part of Springer Nature 2021

## Abstract

Replacement reactions occur during metamorphism and metasomatism in response to changes in pressure, temperature and bulk rock and fluid compositions. To interpret the changes in conditions, it is necessary to understand what phases have previously been present in the rocks. During fluid-mediated replacement, the crystallography of the replacement phases is often controlled by the parent reactant phase. However, excessive fluid fluxing can also lead to extreme element mobility. Titanium is not mobile under a wide range of fluid compositions and so titanium-bearing phases present an opportunity to interpret conditions from the most extreme alteration. We map orientation relationships between titanium-bearing phases from ore deposits using EBSD and use symmetry arguments and existing relationships to show that completely consumed phases can be inferred in ore deposits.

An ilmenite single crystal from Junction gold deposit is replaced by titanite, rutile and dolomite. The rutile has the following well-documented orientation relationship to the ilmenite

$$[0001]_{\text{ilmenite}} // \langle 100 \rangle_{\text{rutile}} \text{ and } \langle 10\bar{1}0 \rangle_{\text{ilmenite}} // [001]_{\text{rutile}}$$

The anatase is a single crystal and shows a potential orientation relationship

$$[0001]_{\text{ilmenite}} = (0001)_{\text{ilmenite}} // \{211\}_{\text{anatase}} \text{ and } \langle 10\bar{1}0 \rangle_{\text{ilmenite}} // \langle 0\bar{1}1 \rangle_{\text{anatase}}$$

The single crystal orientation and lack of symmetrical equivalent variants suggest nucleation dominates the anatase production. Dolomite grew epitaxially on the ilmenite despite only sharing oxygen atoms suggesting the surface structure is important in dolomite nucleation.

Titanite partially replaced ilmenite during metasomatism at Plutonic gold deposit. The titanite orientation is weakly related to the ilmenite orientation by the following relationship:

$$[0001]_{\text{ilmenite}} // \langle 100 \rangle_{\text{titanite}} \text{ and } \{10\bar{1}0\}_{\text{ilmenite}} // (001)_{\text{titanite}}$$

The prevalence of subgrain boundaries in the titanite suggests multiple nucleation points on an already deformed ilmenite needle leading to the formation of substructure in the absence of deformation.

Existing known topotaxial replacement relationship can be used to infer completely replaced phases using the misorientation distributions of the replacement polycrystals. Orientation modelling for a cubic phase replaced by rutile in a sample from Productora tourmaline breccia complex shows misorientation distributions consistent with

$$\langle 001 \rangle_{\text{Rutile}} // \langle 110 \rangle_{\text{cubic}} \text{ and } \langle 100 \rangle_{\text{Rutile}} // \langle 111 \rangle_{\text{cubic}}$$

Combining this with volume constraints and assuming Ti is immobile, the composition of the cubic phase is constrained as titanomagnetite with 85% ulvospinel. Complex microstructures with domainial preferred orientations can also be used to document the microstructure of replaced phases. An aggregate of rutile grains with two parts that share a common  $\langle 100 \rangle$  axis is interpreted as having replaced a twinned ilmenite grain. Modelling shows that the misorientation distribution for the aggregate is consistent with the above relationship replacing ilmenite with a  $\{10\bar{1}2\}$  twin.

**Keywords** Rutile · Ilmenite · Titanite · EBSD · Replacement · Pseudomorph

## Introduction

Geological environments that undergo protracted metamorphic or metasomatic histories frequently contain multiple stages of mineral replacement. In partially reacted

Communicated by Steven Reddy.

✉ Mark Pearce  
mark.pearce@csiro.au

Extended author information available on the last page of the article

rocks, the phase history can be reconstructed by examining the disequilibrium-phase relationships (Schouten 1946), but as overprinting becomes more complete, the mineralogical evolution becomes obscured. It may be possible to infer the former presence of a phase where replacement is pseudomorphic and the phase being replaced has a diagnostic shape (e.g., dolomite rhombs or icosahedral garnets). Where the replacement is isochemical or has a limited number of mobile components (Korzhinskii 1965), examining the composition of the pseudomorph adds another line of evidence to deciphering the long-lost phases (Lindgren 1912). Further evidence for replaced phases comes from knowing the crystallographic correspondence between the replacing phase and the candidate original phases. Titanium is generally considered to be immobile (MacLean and Kranidiotis 1987) over significant length-scales (a few cm perpendicular to, and < 10 m parallel to veins; Van Baalen 1993) under crustal conditions due to high charge and small ionic radius, and is relatively abundant compared to other high field strength elements. In highly metasomatised systems, Ti-bearing minerals are likely to be present even when many of the other components have been completely stripped from the rock. In this contribution, we examine how crystallographic relationships between grains of Ti-bearing minerals can be used to reconstruct the former presence of different phases that, when used with thermodynamic models of metamorphism and fluid flow, can constrain the pressure–temperature–bulk composition evolution of the rocks.

Whilst the role of contemporaneous dissolution and re-precipitation reactions has been discussed for over 100 years (Lindgren 1912), recent experimental studies have led to a greater understanding of mineral replacement mechanisms especially in fluid-dominated systems (see Putnis 2009 and references therein). Numerous model systems have been investigated with the following generalised outcomes:

- (1) Replacement is effective where the common ion effect links the dissolving and replacing phase. For example, where calcite is replaced by apatite, as calcite dissolves the increased concentration of Ca ions at the reaction interface causes the precipitation of apatite in the presence of dissolved phosphate (Kasioptas et al. 2008).
- (2) Coupling of these reactions and the crystallography of the dissolving and precipitating phases is achieved when the dissolution is the rate-limiting step. The relative rates of these processes are controlled by temperature, fluid chemistry and pH (Xia et al. 2009a, b).
- (3) The volume of the replacement phase is a function of not only the molar volume change for the reaction but also the relative solubilities of the dissolving and precipitating phases (Pollok et al. 2011).

Several of these studies have examined the crystallographic orientation relationships between the reactant and product phases such that crystallographic planes or directions in the product correspond to specific planes or directions in the reactant. For a range of different pairs of phases, where the two phases share symmetry elements, then these often control the crystallography of the new phase (Xia et al. 2009a; Pearce et al. 2013; Etschmann et al. 2014). Even when the symmetry relationships are not fully replicated, the crystallographic structure of the old phase can influence the new one as in the case of analcime replacing leucite (Xia et al. 2009b). During this reaction, the twin morphology of the original leucite is maintained by nanoarrays of analcime crystals. Similar symmetry is not the only condition that must be satisfied. If the mismatch between the reactant and product lattices is too large, as is the case during the sulphidation of magnetite to pyrite (Qian et al. 2010) or the precipitation step is rate-limiting, then the crystallography becomes de-coupled. In the case of calcite reacting to apatite, a preferred orientation is generated but it is related to the reaction front mobility rather than underlying crystallographic replacement (Kasioptas et al. 2011).

Crystallographic correspondence between reactants and products is well established for many solid-state reactions and phase transformations (e.g. Hackenberg 2012 pp. 6–7). Temperature-controlled phase changes in metals are used to control grain's size and shape distributions and achieve desired properties in engineered materials. Knowing the relationships between the reactant and product means that theoretical relationships between different grains of product phase can be determined. For high symmetry materials (e.g. cubic metals), each orientation relationship has numerous symmetric equivalents (Barbosa and Lagoeiro 2010) resulting in many pairs of possible product orientations. The exact numbers involved will depend on the symmetries of the reactant, product and the relationship itself. Once understood, these modelled relationships can then be used to infer the presence and quantify the reactant microstructure (Cayron 2007; Cayron et al. 2010) even if it is completely consumed, thereby provide a powerful tool to interrogate a material's history (Timms et al. 2017; Erickson et al. 2019). For example, knowledge of orientation relationships between zircon and its high-pressure polymorph, reidite (Leroux et al. 1999; Cavosie et al. 2015), can be used to infer that reidite was present and has recrystallised during extreme shock metamorphism associated with a meteorite impact based on the relationships observed in clusters of zircon granules where no zircon is preserved (Cavosie et al. 2016). For lower symmetry materials, the orientation relationships between reactant and product minerals may be less numerous or even unique. Even so, understanding the geometric implications of these reactions can affect the interpretation of rock microstructures. McNamara et al. (2012) showed that topotaxial

replacement of high-pressure pyroxenes with a preferred orientation by amphiboles during eclogite exhumation meant that the amphiboles inherited this preferred orientation. Interpreting the amphibole preferred orientation as a result of crystal plasticity during dynamic exhumation rather than a static overprint leads to an erroneous conclusion about continental collision geodynamics.

In this study, we will apply the idea of deciphering the mineralogical evolution using inherited crystallography, or 'phase heritage' (Timms et al. 2017), to mineralised rocks in highly metasomatised environments. We will focus on Ti-bearing minerals because, as discussed above, Ti is relatively immobile under crustal conditions but relatively abundant in many different rock types. Titanium-bearing minerals, in particular rutile and titanite, can accommodate a number of substitutions of important elements used in mineral exploration and distinguish mineralised from unmineralised rocks in orogenic gold systems (Scott et al. 2011; Plavsa et al. 2018; Agangi et al. 2019). More widely, the stability of the Ti-phase ilmenite, rutile and titanite (along with the metastable TiO<sub>2</sub> polymorphs brookite and anatase) can be used to interpret conditions, such as temperature, pH and metasomatizing fluid chemistry (Angiboust and Harlov 2017 and references therein). The different polymorphs of TiO<sub>2</sub> have different affinities for trace elements (Triebold et al. 2011) that are routinely used to interpret geological history (e.g. Nb in rutile; Ryerson and Watson 1987). Although these interpretations remain contentious because geochemical proxies cannot be verified by direct observation (Baier et al. 2008), knowledge of how trace element host phases evolve during geologic processes will exert a first-order control on the ultimate trace element patterns in rocks. The usefulness of Ti-bearing phases will be extended further into the mantle and extreme environments like meteorite impacts as more is learnt about the high-pressure TiO<sub>2</sub> polymorphs, Akaogiite (Goresy et al. 2010) and  $\alpha$ -PbO<sub>2</sub> structured TiO<sub>2</sub> (Hwang et al. 2000).

## Methods

A number of methods exist to measure crystallographic orientation but the most common are based on diffraction of electrons, X-rays or neutrons. Studies of twin formation and exsolution, which seek to quantify orientation relationships precisely, use transmission electron microscope (TEM)-based imaging and electron diffraction to measure the orientations of the adjacent crystals whilst also imaging the interface (Wang et al. 1990; Rečnik et al. 2015). Electron backscatter diffraction (EBSD) in the scanning electron microscope (SEM) is used to measure the crystallographic orientation across a much larger field of view than is possible in a TEM and can provide orientation relationships from

a statistically representative number of grains but without the precision of a TEM. In this study, the Ti-bearing-phase orientations are measured using EBSD. Measurements from adjacent pixels are used to quantify orientation relationships in detail whilst bulk data are obtained from the EBSD maps.

## Electron backscatter diffraction

Electron backscatter diffraction is used to measure the orientation of crystalline materials. Maps of orientation variation are constructed by recording a grid of points (Prior et al. 1999) with a typical spatial resolution of ~60 nm. Kikuchi diffraction patterns, which result from diffraction of the incident electron beam according to the Bragg equation, are imaged on a phosphor screen by a low-light charge-coupled device (CCD) camera or complementary metal-oxide-semiconductor (CMOS) sensor. These patterns are indexed against a user-defined library of possible phases to give the orientation of that point and the corresponding phase. Phases with similar crystallography but different chemistry (e.g. pyrite and gold) produce similar but subtly different diffraction patterns that can be challenging to discriminate during fast automated acquisition. In this case, contemporaneous energy-dispersive X-ray (EDX) spectra can also be used to discriminate between the phases while maintaining fast data acquisition speed.

In this study, the EBSD datasets were collected using a Zeiss UltraPlus field emission gun SEM equipped with a Bruker e<sup>-</sup>Flash HR EBSD detector and a Bruker xFlash EDX detector both controlled using Bruker Esprit v2.1. The SEM was operated at 20 keV accelerating voltage and 12.1 nA beam current for all maps. The step sizes between measurements were chosen to depict the microstructures of interest and the dwell times, the time to collect a single diffraction pattern, were varied to give good results for different phases. These parameters are shown in Table 1. Orientation and phase data were exported as ASCII Channel text files (.ctf) and processed using EBSDInterp v.1 (Pearce 2015a, b) to interpolate missing measurements using microstructural constraints to avoid artefacts (Prior et al. 2009; Pearce 2015b). The processed datasets were imported into Oxford Instruments-HKL CHANNEL5 (service pack 10) to analyse the maps and orientation data. EBSD can distinguish all the polymorphs of TiO<sub>2</sub> because they have sufficiently distinct unit cells. The unit cells data used for the EBSD mapping are shown in Table 1.

## EBSD data presentation

EBSD datasets can be presented as a bulk measure of crystallographic preferred orientation (CPO) or maps to analyse spatial variations in crystallographic orientation. Bulk data are presented as pole figures, equal area stereograms, where each

**Table 1** EBSD map step size and unit cells used for the different datasets analysed in this paper

Figure	Step size (nm)	Phase	Crystal system	Laue class	<i>a</i> (Å)	<i>b</i> (Å)	<i>c</i> (Å)	$\alpha$ (°)	$\beta$ (°)	$\gamma$ (°)
1	490	Rutile	Tetragonal	4/mmm	4.6	4.6	3.0	90	90	90
		Mg-Calcite	Trigonal	$\bar{3}m$	5.0	5.0	17.0	90	90	120
		Anatase	Tetragonal	4/mmm	3.8	3.8	9.5	90	90	90
		Ilmenite	Trigonal	$\bar{3}m$	5.1	5.1	14.0	90	90	120
		Quartz	Trigonal	$\bar{3}m$	4.9	4.9	5.4	90	90	120
2	806	Ilmenite	Trigonal	$\bar{3}m$	5.1	5.1	14.0	90	90	120
		Titanite	Monoclinic	2/m	6.5	8.7	7.1	90	113.9	90
		Quartz	Trigonal	$\bar{3}m$	4.9	4.9	5.4	90	90	120
3	239	Rutile	Tetragonal	4/mmm	4.6	4.6	3.0	90	90	90
		Quartz	Trigonal	$\bar{3}m$	4.9	4.9	5.4	90	90	120
		Glaucanite (Muscovite)	Monoclinic	2/m	5.3	9.1	10.2	90	78.9	90
		Sanidine (K-feldspar)	Monoclinic	2/m	8.7	13.0	7.2	90	64.27	90
6	184	Pyrite	Cubic	$m\bar{3}$	5.3	5.3	5.3	90	90	90
		Rutile	Tetragonal	4/mmm	4.6	4.6	3.0	90	90	90
		Schorl	Trigonal	$\bar{3}m$	16.0	16.0	7.2	90	90	120
		Quartz	Trigonal	$\bar{3}m$	4.9	4.9	5.4	90	90	120
		Muscovite	Monoclinic	2/m	5.2	9.0	20.1	90	95.8	90
		Chalcopyrite	Cubic	$m3m$	5.2	5.2	5.2	90	90	90
		Sanidine (K-feldspar)	Monoclinic	2/m	8.6	13.0	7.2	90	116	90

point represents a measurement. A pole figure is presented for each crystallographic axis or pole to plane that aggregates all the measurements from a set or subset of data. For large datasets, the density of data points is contoured, using an optimised de la Vallee Poussin kernel (Schaeber 1997) computed by MTEX (Bachmann et al. 2010), and the contour values are multiples of a uniform (random) distribution that show semi-quantitatively how clustered the data are. Contoured data are presented using the perceptually uniform colourmap, davos (Crameri 2018). These colourmaps do not emphasise particular intervals of contours and therefore provide the viewer with a fairer comparison of cluster size (in this case the angular variation) between different datasets (see Crameri et al. 2020 for a recent discussion). In the spatial data, grains are defined by changes in orientation between pixels that are larger than a threshold value, typically  $10^\circ$ . Within a given grain, the orientation variation between points records the intra-granular lattice bending accommodated by crystal plasticity (Lloyd et al. 1997; Prior et al. 2002) and/or microfracturing (Vernooij et al. 2006). Relationships between grains can be used to interpret the activation of processes, such as dynamic recrystallization (Halfpenny et al. 2006), twinning (Bestmann and Prior 2003) and topotaxial replacement (Pearce et al. 2013).

### Crystallographic notation

Standard crystallographic notation for Miller (phases in crystal systems other than trigonal) and Miller-Bravais

(trigonal phases, based on a hexagonal unit cell) indices is used throughout this paper. Single-zone axes (directions) are denoted by square brackets []; symmetrically equivalent groups of zone axes are denoted using triangular brackets  $\langle \rangle$ ; single planes (shown on pole figures as poles to planes) are denoted by parentheses (); symmetrically equivalent groups of planes are shown as curly braces {}. For high symmetry phases (e.g. cubic), pole figures contain multiple planes/zone axes because there are many symmetric equivalents. With decreasing symmetry, the number of zone axes/pole in a group decreases such that in, for example, monoclinic crystals, the maximum number of symmetrical equivalent directions any group contains is 2. Another important point to note is that in high symmetry materials, some (or all) directions are perpendicular to the plane with the equivalent indices, e.g.  $\langle 111 \rangle$  is perpendicular to  $\{111\}$ . With decreasing symmetry, this is generally not true and so care must be paid to whether poles to planes or zone axes are being plotted as they are not interchangeable.

### Orientation definitions

Crystallographic orientations are defined in EBSD datasets as a rotation of the crystal relative to the sample. The rotations are expressed using two sets of Cartesian co-ordinate systems, the sample co-ordinate system aligned with the horizontal and vertical edges of the map and the sample surface normal, *X*, *Y*, and *Z*, respectively, and the crystal

co-ordinate system aligned with the principle crystal directions  $X_i$ ,  $Y_i$  and  $Z_i$ . For crystal systems with non-orthonormal principle crystallographic directions (monoclinic, triclinic, trigonal), not all the principle directions can be parallel to the orthonormal co-ordinate systems axes, so a relationship between the two reference frames (crystal axes and crystal co-ordinates) must follow a predefined convention. This study follows the convention adopted by the CHANNEL5 software that [001] is parallel to  $Z$  and the reciprocal-space  $a^*$  axis (the normal to the plane containing the  $b$  and  $c$  crystal axes) is parallel to  $X$ . This common definition of the relationship between the crystallographic axes and the crystal orthonormal basis vectors means that it is possible to define relationships between crystals of different Laue classes by defining the rotation that maps one co-ordinate system into the other. For example, if during a reaction, a cubic mineral is replaced by a monoclinic one with the relationship,

$$[001]_{\text{cubic}} // [001]_{\text{monoclinic}} \text{ and } (110)_{\text{cubic}} // (100)_{\text{monoclinic}}$$

then this relationship can be thought of as a  $45^\circ$  rotation around the  $c$ -axis of the monoclinic phase to transform it from the reference orientation into the orientation of the cubic phase. This concept of calculating the rotations between two reference orientations both aligned with orthonormal crystal co-ordinate systems forms the basis of 3D misorientation space analysis (Krakow et al. 2017) as discussed below. The calculations here are implemented using the open-source Matlab toolbox software MTEX (Bachmann et al. 2010) and so the rotation conventions used are those that are adopted by MTEX:

- 1) Rotations are defined as positive anti-clockwise around an axis looking down the axis towards the origin
- 2) Rotations are defined as mapping the crystal reference frame into the sample reference frame

Rotations can be defined as rotation axis-angle pairs, rotation matrices, quaternions, or sets of Euler angles, which are the angular rotations around a sequence of axes defined by convention (Cho et al. 2005). The data can be converted between these definitions using equations, such as those presented by Cho et al. (2005) summarising the results of Bunge (1982, pp. 19–22) and Humbert et al. (1996). In this study, the rotation calculations are presented as matrix operations because this makes the problems tractable with relatively simple linear algebra although the MTEX implementation uses the quaternion equivalents. Data are discussed as axis-angle pairs, which describe the rotation of one crystal around a particular axis, defined in the crystal reference frame, by a specified angle to bring it into coincidence with a second crystal. This description is used because this form of rotation definition allows the key crystallographic elements to be more easily defined (as they are often low-index directions and planes) and is often more intuitive when thinking about minerals of different crystal systems.

## Misorientations

The most commonly used description of intergranular relationships in the Earth sciences is misorientation, which describes the transformation from one orientation to another in terms of a rotation by a given angle about a rotation axis that is defined either in the crystal reference frame or the sample reference frame (Mainprice et al. 1993). The rotation axis is, by definition, the axis of zero displacement during the rotation operation and therefore remains in the same orientation in both sample and crystal reference frames. Due to crystal symmetry, each pair of orientations can, in general, be described by more than one rotation. The disorientation convention (Mackenzie and Thomson 1957) is used to select the misorientation from the set of misorientations that has the lowest rotation angle. Misorientations between pairs of measurements in a map can be compiled into a misorientation distribution histogram (Pospiech et al. 1986). The pairs are chosen as adjacent pixels or randomly selected pairs of measurements from anywhere within the map. Adjacent or neighbour pair distributions are influenced by processes that cause alignment of adjacent grains whereas the random pair distributions describe the whole aggregate (Wheeler et al. 2001). To account for variations in boundary topology and grain size, EBSD maps presented here have been subsampled as one pair of points per grain boundary before being presented in the misorientation distribution plots.

An alternative visualisation of misorientation distributions, the misorientation space that examines both rotation axis and angle but neglects relative intensity within a distribution was proposed by Krakow et al (2017). The authors' treatment of misorientation data is to construct a fundamental region within which bounds all possible disorientations between two crystals of potentially different Laue class. The disorientations are calculated assuming a reference orientation, which in this case follows the convention outlined above ( $c$ -axis //  $Z$ ,  $a^*$ -axis parallel to  $x$ ) for all Laue classes. Misorientations are visualised as vectors where the orientation is the rotation axis and the length is proportional to the misorientation angle. Multiple misorientations are visualised by plotting a single dot whose polar co-ordinates (direction and length) represent a single misorientation. Clouds of dots represent clusters of similar misorientations (analogous to peaks in the misorientation angle distribution) both in angle and axis and the spread is a measure of how 'specific' or 'dispersed' the crystallographic orientation relationship is (Habler and Griffiths 2017). Rotational relationships will be oriented along lines in misorientation space. This representation is used below to compare predicted maxima in misorientation distributions with experimental results. The predicted maxima are specific orientation relationships and therefore show no spread.



Data and Matlab scripts for use with MTEX to reproduce the figures in this paper can be downloaded from the CSIRO Data Repository (Pearce 2020).

## Case study results

The reaction microstructures involving Ti-bearing phases presented here are taken from three different ore deposits. Each of these deposits is briefly described in turn to give context to the microstructural data that are presented subsequently.

### Ilmenite breakdown, Junction Gold Mine, Kambalda, Western Australia

The Junction gold deposit is an Archean greenstone hosted gold deposit hosted in the Junction dolerite sill in the St Ives camp near Kambalda. The host rocks exhibit igneous differentiation with the majority of the gold hosted in the Fe- and Ti-rich parts of the sill (Carey 1994). The Junction dolerite is chemically similar to the Condenser and Golden Mile dolerites, both of which host large gold deposits. Fluid flow through the Junction dolerite was promoted by fractures associated with the Junction shear zone, a splay of the nearby Boulder-Lefroy fault, and syn-mineralisation veins are associated with a mineralogically zoned alteration halo that exhibits evidence for multiple stages of mineral replacement reactions during progressive fluid–rock interaction.

With increasing alteration intensity, the metamorphic assemblage of amphibole, albite, epidote, chlorite and quartz is replaced by increasing amounts of biotite and chlorite, and there is a significant increase in pyrrhotite and carbonate minerals. In igneous zone 3, the zone most enriched in Fe and Ti, igneous titanomagnetite is replaced by ilmenite and magnetite probably during oxidation and cooling of the sill (Polito et al. 2001). These have in turn been replaced by pyrrhotite ± pyrite in the most altered parts of the system. The sample examined here is taken from igneous zone 3 (sample 250 of Polito et al. 2001; see their Fig. 3) and contains an alteration assemblage biotite, chlorite, calcite, albite, ilmenite and pyrrhotite. Late-stage fluid flow associated with gold mineralisation (Pearce et al. 2015) has led to Fe mobility at the thin-section scale such that ilmenite and biotite were broken down and early-formed calcite has been replaced by dolomite and siderite (Pearce et al. 2013). The focus of this study is a single-needle-shaped crystal of ilmenite that has been partially replaced by TiO<sub>2</sub> phases and dolomite (Fig. 1).

The ilmenite needle in the sample from the Junction gold mine has partially broken down to anatase and rutile, two different polymorphs of TiO<sub>2</sub>. Anatase, which forms a blocky crystal (green in Fig. 1a) with a uniform crystallographic orientation (uniform colour in Fig. 1b), has replaced

the majority of the ilmenite. Rutile is much finer-grained than anatase and is restricted to the margins of the needle, dominantly the near the phase boundary between the ilmenite needle and biotite (red in Fig. 1a). The rutile crystals occur in different orientations (Fig. 1d) and these different orientations are spatially mixed rather than forming discrete domains. By rotating the data into standard reference frame of the reactant mineral, it is often easier to see which directions line up because the clusters of orientation appear on the primitive of the stereogram and at regular intervals within the pole figure (Fig. 1d–g). The three orientations are not random but all share a  $\langle 100 \rangle$  direction (Fig. 1e) and are misoriented from each other by 60°. The  $\langle 100 \rangle$  directions perpendicular to the shared  $\langle 100 \rangle$  direction (rutile is tetragonal and therefore  $\langle 100 \rangle = \langle 010 \rangle$ ) are distributed regularly at 60° intervals in the plane perpendicular to the shared  $\langle 100 \rangle$  direction. Comparing the rutile orientations to the orientation of the original ilmenite needle, it can be seen by inspection that the shared rutile  $\langle 100 \rangle$  direction is parallel to the ilmenite  $c$ -axis  $[0001]$  and because of tetragonal symmetry of rutile  $\{100\}$  is parallel to the basal plane of ilmenite  $(0001)$ . The  $[001]$  directions of rutile are parallel to the  $m$  directions  $\langle 10\bar{1}0 \rangle$  of ilmenite. From these data, it is inferred that the ilmenite-to-rutile reaction proceeds by topotaxial replacement with the following orientation relationship:

$$[0001]_{\text{ilmenite}} // \langle 100 \rangle_{\text{rutile}} \text{ and } \langle 10\bar{1}0 \rangle_{\text{ilmenite}} // [001]_{\text{rutile}}$$

Due to the orthogonality between crystal directions in both phases, the following is also true:

$$\langle 110 \rangle_{\text{ilmenite}} // \langle 100 \rangle_{\text{rutile}}$$

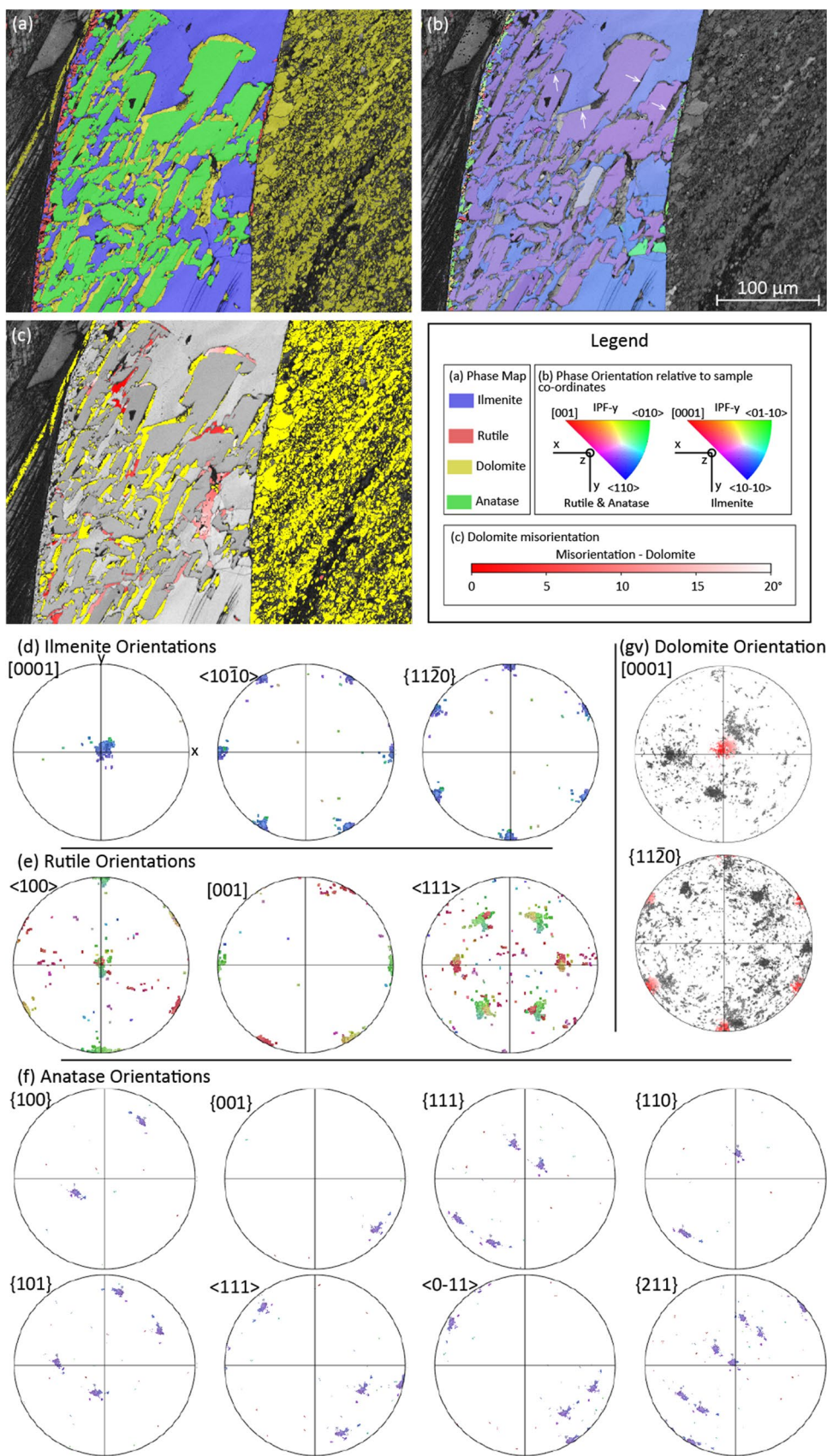
Anatase has grown as a single crystal within the ilmenite needle shown by the relatively uniform orientation in Fig. 1b. The anatase has euhedral crystal faces (indicated by white arrows on Fig. 1b) and contains a few low-angle grain boundaries. The orientation relationship between the ilmenite and the anatase is not as clear as that between the ilmenite and the rutile. Inspection suggests that the following relationship:

$$[0001]_{\text{ilmenite}} = (0001)_{\text{ilmenite}} // \{211\}_{\text{anatase}} \text{ and } \langle 10\bar{1}0 \rangle_{\text{ilmenite}} // \langle 0\bar{1}1 \rangle_{\text{anatase}}$$

A second  $\{211\}_{\text{anatase}}$  plane appears to be parallel to  $\langle 10\bar{1}0 \rangle_{\text{ilmenite}}$  but strictly the two symmetrically equivalent  $\{211\}_{\text{anatase}}$  planes are 91.8° apart so cannot both strictly be parallel to ilmenite directions that are 90° apart, although it is impossible to tell which is correct with spread in reactant orientations observed here.

The reaction from ilmenite to anatase, and the other TiO<sub>2</sub> polymorphs, releases iron. Where the iron is removed from the local system by fluid movement through the rocks, this results in a negative volume change of reaction. It should be noted that the iron can be moved over a short distance and re-precipitated as is the case at Junction with siderite veins, but does not form a major part of the ilmenite pseudomorph.

**Fig. 1** EBSD data showing replacement of an ilmenite single crystal by  $\text{TiO}_2$  and dolomite. Pole figures are shown with data rotated into the ilmenite reference orientation not in sample co-ordinates. **a** EBSD phase map with the ilmenite (blue) needle being replaced by both anatase (green) and rutile (red). The volume lost due to Fe mobility is filled with dolomite (yellow). **b** Orientation data showing that the ilmenite, coloured relative to the mean ilmenite orientation, and the anatase, coloured using an inverse pole figure colour scheme showing which crystal direction is parallel to the sample Y-axis, are both single crystals. White arrows indicate euhedral crystal faces. **c** Relative misorientation map showing dolomite orientations within  $20^\circ$  of the ilmenite orientation (both minerals are space group R). Dolomite misoriented by  $>20^\circ$  is coloured yellow. Much of the dolomite filling the porosity created during ilmenite breakdown is misoriented  $<20^\circ$  from the ilmenite. The reference orientation used for the dolomite is the mean ilmenite orientation that has Euler angles 80.4, 56.3, and 291.4. **d** Pole figures for ilmenite orientations coloured using the colour scheme in **(b)**. **e** Rutile orientations coloured as in **(b)**. **f** Anatase orientations coloured using the same colour scheme in **(b)**. **g** Dolomite orientations coloured to show the grains that are misoriented  $<20^\circ$  from the mean ilmenite orientation (as in **c**). Other orientations are grey.





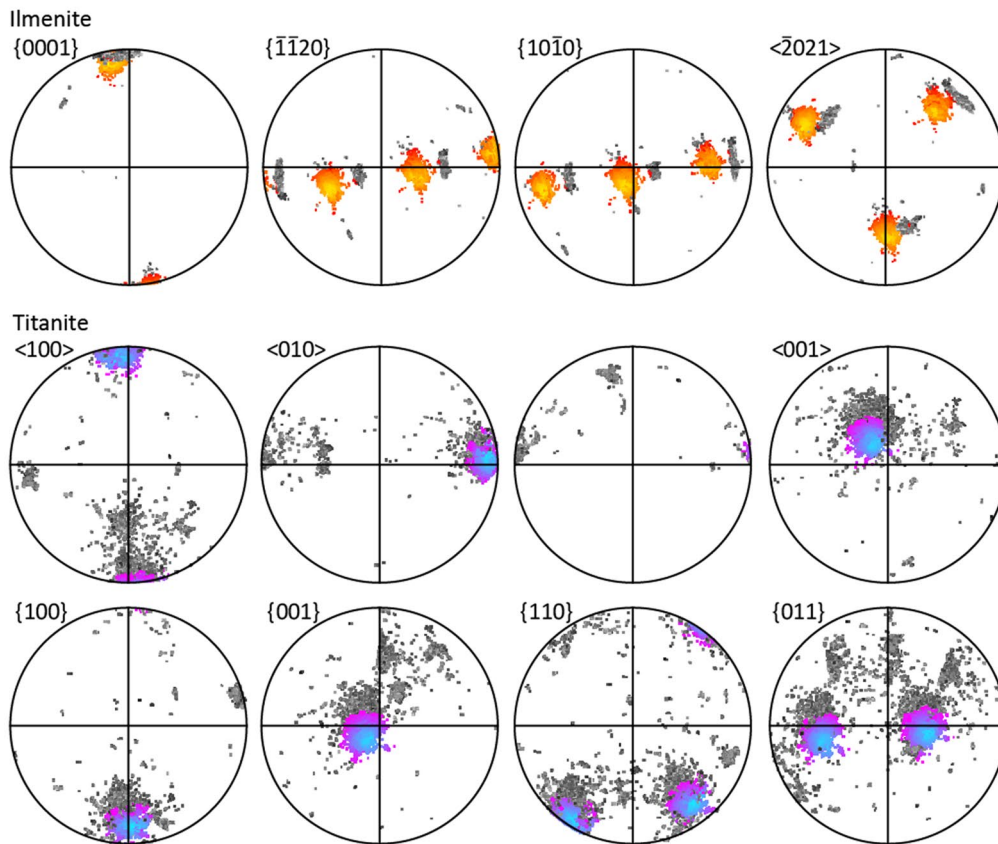
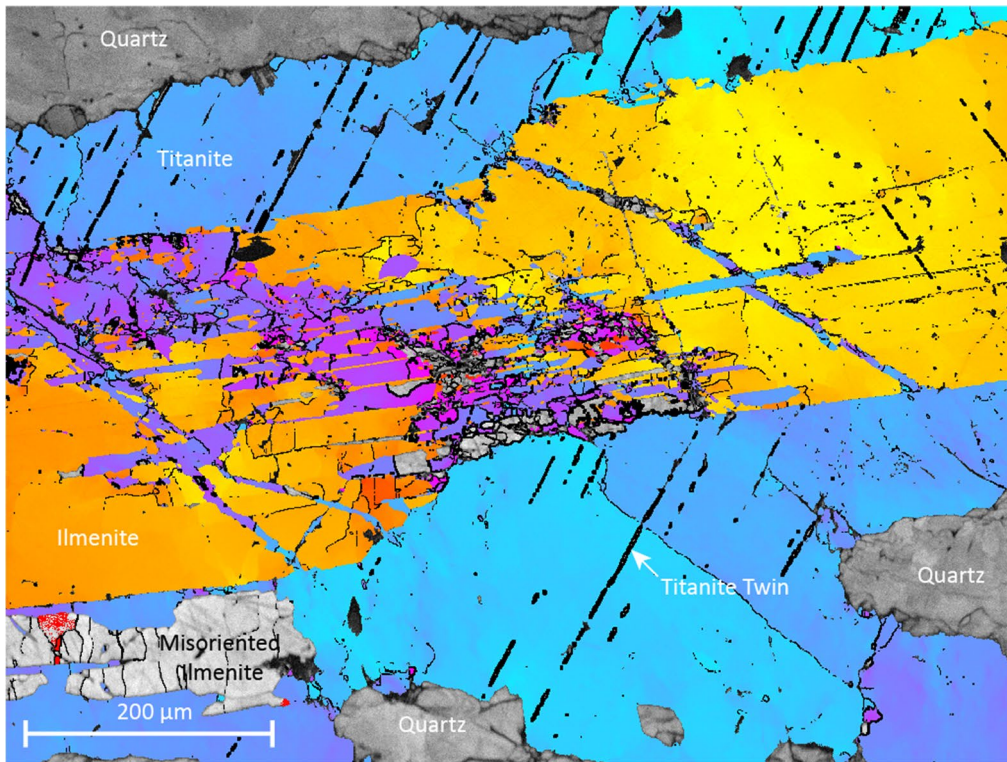




**Fig. 2** EBSD data showing titanite replacing ilmenite in Plutonic Gold Mine, Western Australia. **a** Relative misorientation map showing misorientation in titanite (blue to pink) and ilmenite (yellow to red) relative to the crystallographic orientation of ilmenite at  $X_j$ , and the theoretical titanite based on the observed orientation relationship. Thin black lines are boundaries with misorientation angles  $> 2^\circ$  and thick black lines are boundaries with misorientation angles  $> 10^\circ$ . **b** Orientation data for ilmenite presented as pole figures with the same colour scheme as (a). **c** Orientation data for titanite presented as pole figures with the same colour scheme as (a)

In the microstructure study, the porosity generated during reaction is concentrated at the reaction interface and is filled with dolomite (Fig. 1a). The vein margin adjacent to the ilmenite needle is also composed of fine-grained dolomite (right and side of Fig. 1). A direct comparison is possible between these two minerals because they are both of the same space group (R). Comparing the dolomite orientations to that of the ilmenite needle (Fig. 1c) shows that many of the dolomite grains that form in the reaction interface are misoriented at  $< 20^\circ$  to the mean ilmenite orientation (red to white in Fig. 1c and see pole figures in Fig. 1g). In contrast to the dolomite grains in the reaction interface, the dolomite in the adjacent veins shown little coincidence in orientation with the ilmenite needle.

### Ilmenite–titanite reaction, Plutonic Gold Mine, Western Australia

Plutonic Gold mine is located in the Marymia Inlier between the Yilgarn and Pilbara cratons in Western Australia. The rocks that host the gold deposit are a sequence of metamorphosed basalts and volcanoclastic sediments that experienced middle amphibolite facies metamorphism around  $600^\circ\text{C}$  and 8 kbar (Gazley et al. 2011, 2014) followed by greenschist facies overprint. Gold is found within early arsenopyrite and as native metal associated with epidote alteration of the metamorphic amphiboles (Gazley et al. 2011). During this retrogression, igneous to early metamorphic ilmenite is replaced by titanite. During metamorphism of basaltic rocks, titanite is generally stable at greenschist-lower amphibolite facies and is replaced by ilmenite at higher temperatures and rutile at higher pressure (e.g. Diener and Powell 2012 Fig. 1 calculations using MORB composition). The replacement of an ilmenite needle by metamorphic titanite is the focus of the second case study.

Ilmenite breakdown to titanite has been recorded using EBSD and the data are presented in Fig. 2. The ilmenite was initially a needle oriented with the long axis subparallel to horizontal in the figure. This is manifested in the crystallographic orientation data by the ilmenite basal plane being oriented subparallel to the horizontal in the figure (Fig. 2b). Both the ilmenite and the titanite that is replacing it show internal orientation variation highlighted by colour variation

in both phases in Fig. 2a. The ilmenite contains boundaries with traces parallel and perpendicular to the basal plane. Titanite contains twins outside the margins of the original ilmenite grain but also cuts across the ilmenite needle. In the zone where it cross-cuts the ilmenite, the titanite contains low-angle boundaries and a spread of orientations including some grains that are by greater than  $20^\circ$  from the reference value (displayed as grey in Fig. 2). The misorientation of  $20^\circ$  was selected because this is the magnitude of orientation variation within the reactant ilmenite needle. The majority of the titanite that occurs outside of the original ilmenite outline has a very similar orientation within 8 degrees of the reference orientation. Most of the grains that occur within the cross-cutting zone are outside of this orientation.

The crystallographic orientation data for the ilmenite and titanite from Plutonic show much simpler crystallography than the rutile datasets examined previously. A single ilmenite orientation (with a second grain that is not volumetrically significant) has been replaced by titanite that shows a restricted range of orientations. This allows the following orientation relationships to be inferred:

$$[0001]_{\text{ilmenite}} // \langle 100 \rangle_{\text{titanite}} \text{ and } \{10\bar{1}0\}_{\text{ilmenite}} // (001)_{\text{titanite}}$$

Due to the orthogonality of these two directions in the monoclinic titanite, the third mutually perpendicular direction is also related to a rational direction in the ilmenite,

$$\langle 010 \rangle_{\text{titanite}} = (010)_{\text{titanite}} // \{\bar{1}\bar{1}20\}_{\text{ilmenite}}$$

This orientation relationship was combined with the mean orientation of the ilmenite needle to predict the reference orientation for the titanite in Fig. 2a. The close correspondence of the majority of the titanite within  $20^\circ$  of the theoretical titanite orientation based on the above orientation relationship gives confidence in that relationship even though it was identified empirically from the map.

### Rutile aggregates, Productora Cu–Au–Mo deposit, Chile

The Productora Cu–Au–Mo deposit occurs within a magmatic-hydrothermal breccia complex in the Coastal Cordillera of northern Chile. The host rocks are massive, crystal-rich, lapilli tuffs of dacite to rhyolite composition. Multiple brecciation events have led to widespread and intense alteration mineralogy (Escolme 2017; Escolme et al. 2020). The Cu–Au–Mo mineralisation is associated with tourmaline–pyrite–chalcopyrite  $\pm$  magnetite  $\pm$  biotite–cemented hydrothermal breccias with intense K-feldspar alteration. The mineralised breccias overprint earlier intense quartz–pyrite–cemented breccias with muscovite alteration, and local kaolinite–muscovite–pyrite alteration. The sample studied here has been intensely altered by all these events.

The orientations of grains from two aggregates of rutile from the Productora deposit were mapped using EBSD. In contrast to the other examples illustrated, there is no reactant

mineral remaining, so symmetry arguments and evidence from the other case-studies will be employed to infer the original mineralogy. The first ‘aggregate’ is sparsely distributed but the individual grains are arranged in a truncated triangular region (Fig. 3a). The matrix of this rutile aggregate is composed of a Fe-bearing white mica (mapped using a glauconite match unit as this was found to be the closest match by testing multiple points using an automated

routine in the Bruker Esprit software to test multiple phases) and quartz with a higher proportion of white mica within the aggregate than outside the margin (Fig. 3a). The rutile aggregates themselves are arranged either as anhedral aggregates or as linear arrays of grains that are parallel to the margins of the triangular domain (Fig. 3b).

Pole figures show a range of orientations (Fig. 3c) but are clustered and do not have a random distribution.

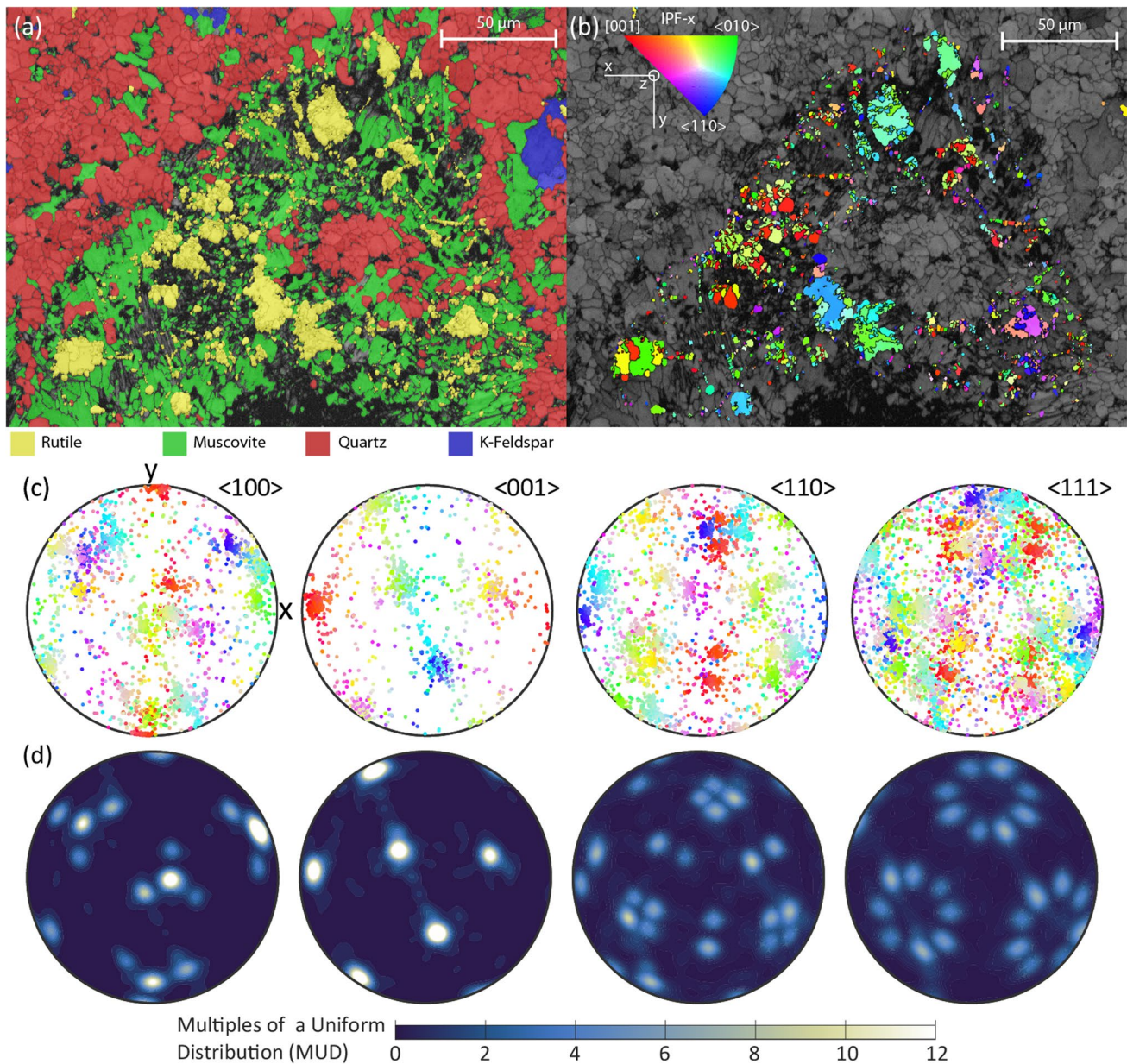


**Fig. 3** EBSD data of a euhedral rutile aggregate from Productora, Chile. **a** Phase map showing the distribution of white mica in a truncated triangular shape that contains the rutile. **b** EBSD orientation map showing the variation in orientation between rutile grains and within the larger aggregates. **c** Raw data as stereograms coloured using the same colour scheme as Fig. 3 showing clustering in

the data. **d** Contoured versions of the data from (c) shows a systematic pattern in the clustering with four major clusters in  $\langle 100 \rangle$ , six in  $\langle 001 \rangle$  and three in  $\langle 110 \rangle$  with other minor clusters. Contours are coloured according to the multiples of uniform distribution (all with the same scale)



Contouring the raw data reveals a systematic pattern that has multiple maxima for each of the crystallographic directions. The  $\langle 100 \rangle$  directions have four maxima with some minor dispersion around the edges of the clusters. Two of the clusters appear to be pairs of maxima with the other two maxima more concentrated (higher contour values). The  $\langle 001 \rangle$  directions have six maxima distributed across the pole figure. The  $\langle 111 \rangle$  pole figure shows three circles of orientations each of which is centred on a major  $\langle 110 \rangle$  cluster. In addition to the major clusters in the  $\langle 110 \rangle$  pole figure, there are subsidiary clusters that have the same symmetry as the major clusters.

The symmetry and multiplicity of these clusters in the different pole figures are not consistent with a tetragonal mineral (e.g. two clusters of  $\langle 100 \rangle$  directions for each one  $\langle 001 \rangle$ ) suggesting that there is an external control on the orientation data. Combining the multiplicities from each of the pole Figs. ( $4 \times \langle 100 \rangle$ ,  $6 \times \langle 001 \rangle$  and  $3 \times \langle 110 \rangle$ ) shows that, overall, the rutile data have the symmetry elements of a cubic mineral. Therefore, it is likely that the rutile grains shown here are replacing a grain of a cubic mineral where  $\langle 100 \rangle_{\text{Rutile}} // \langle 111 \rangle_{\text{cubic}}$ ,  $\langle 001 \rangle_{\text{Rutile}} // \langle 110 \rangle_{\text{cubic}}$ ,  $\langle 110 \rangle_{\text{Rutile}} // \langle 001 \rangle_{\text{cubic}}$ . Furthermore, in face-centered cubic minerals, the  $\{111\}$  plane is the hexagonal close packed plane and often forms truncated triangular crystals with a crystal habit similar to the euhedral aggregate in Fig. 3a. This is consistent with the triad symmetry axis of the rutile preferred orientation that is orientated perpendicular to the plane of the section (in the centre of the stereogram). However, not all of these relationships interpreted from the symmetry arguments can be strictly true because of the angular differences between the orientations. The angle between  $\langle 110 \rangle$  and  $\langle 100 \rangle$  in rutile is  $45^\circ$  and the angle between  $\langle 001 \rangle$  and  $\langle 111 \rangle$  in cubic phases is  $\text{atan}(\sqrt{2}) = 57.4^\circ$ . Therefore, both relationships cannot be true so we will explore which is supported by the data.

The intensity and clustering of the  $\langle 001 \rangle_{\text{Rutile}}$  poles shows that this is strongly controlled during the replacement. The other two pole figures show less well clustered maxima but combining each of the remaining two possible relationships with  $\langle 001 \rangle_{\text{Rutile}} // \langle 110 \rangle_{\text{cubic}}$  defines two potential orientations relationships:

OR-1  $\langle 001 \rangle_{\text{Rutile}} // \langle 110 \rangle_{\text{cubic}}$  and  $\langle 110 \rangle_{\text{Rutile}} // \langle 001 \rangle_{\text{cubic}}$  and

OR-2  $\langle 001 \rangle_{\text{Rutile}} // \langle 110 \rangle_{\text{cubic}}$  and  $\langle 100 \rangle_{\text{Rutile}} // \langle 111 \rangle_{\text{cubic}}$ .

Using these two relationships, orientation relationship matrices can be constructed that transform the rutile relationship to its cubic counterpart. Where the minerals have similar crystallography and the relationships are simple between principal directions, then these matrices may be constructed by inspection. Where their crystal structures are not at all similar, it may be necessary to use algebraic

methods or existing software (e.g. Angel et al. 2015) to calculate the orientation relationship matrix, the general case of which is described in the Appendix.

Due to the symmetry of rutile and cubic minerals, each of these relationships results in multiple possible crystal orientations for a single starting orientation. Therefore, for a single starting cubic orientation, the set of symmetrically equivalent rutile orientations produced during reaction can be calculated and their misorientation distribution simulated (assuming all symmetric equivalents are equally likely). These simulations are shown in Fig. 4 for the EBSD map in Fig. 3. The two orientation relationships produce different distributions of misorientations where OR-1 has a large peak at around  $63^\circ$  with a smaller peak at  $90^\circ$ . The peaks at  $63^\circ$  and  $90^\circ$  are still present for OR-2, but there are subsidiary peaks at  $60^\circ$ ,  $70^\circ$  and  $20^\circ$ . Comparing this to the random pair histogram (red in Fig. 4b) for the experimental data shows that the frequency histogram matches OR-2 better than the more straightforward distribution of misorientations obtained from OR-1. The neighbour pair relationships are dominated by a peak around  $60^\circ$  and have subsidiary peaks at around  $30^\circ$  and  $40^\circ$ .

The same two orientation relationships have been modelled using the 3D misorientation space method (Krakow et al. 2017) to test not only the key misorientation angles between product phases (which are reproduced by the misorientation angle distribution modelling discussed above) but also the axes (Fig. 4c). The clusters of data in the misorientation space correspond to the peaks in the misorientation angle distributions and match predicted specific misorientations from OR-1. This result further strengthens OR-1 as the relationship that controls this microstructure because the misorientation distributions between the products match the axis, angle and relative frequency of angle distributions in the observed data.

A second rutile aggregate from the Productora deposit contains two different domains based on grain orientation (Fig. 5). These two domains are potentially derived from different crystals but the orientation data show that they share a  $\langle 100 \rangle$  direction (highlighted by the red circle in Fig. 5b). Treating the two parts of the aggregate separately, the orientation patterns appear similar to those in Fig. 1d. Both are composed of multiple sets of orientations where the grains within the set all share a common  $\langle 100 \rangle$  direction and are misoriented by  $60^\circ$  to each other. The two different sets (subsets 1 and 2) outlined in Fig. 5a share a  $\langle 100 \rangle$  direction that is not shared by the individual members of the two sets. The misorientation distribution shows large peaks at  $60^\circ$  in both the random and neighbour pair distributions (Fig. 6). There are also minor peaks and low angles and at  $45^\circ$ ,  $54^\circ$  and  $85^\circ$  in the random pair distribution and smaller peaks at  $20^\circ$ ,  $30^\circ$  and  $40^\circ$  in the neighbour pair distribution.



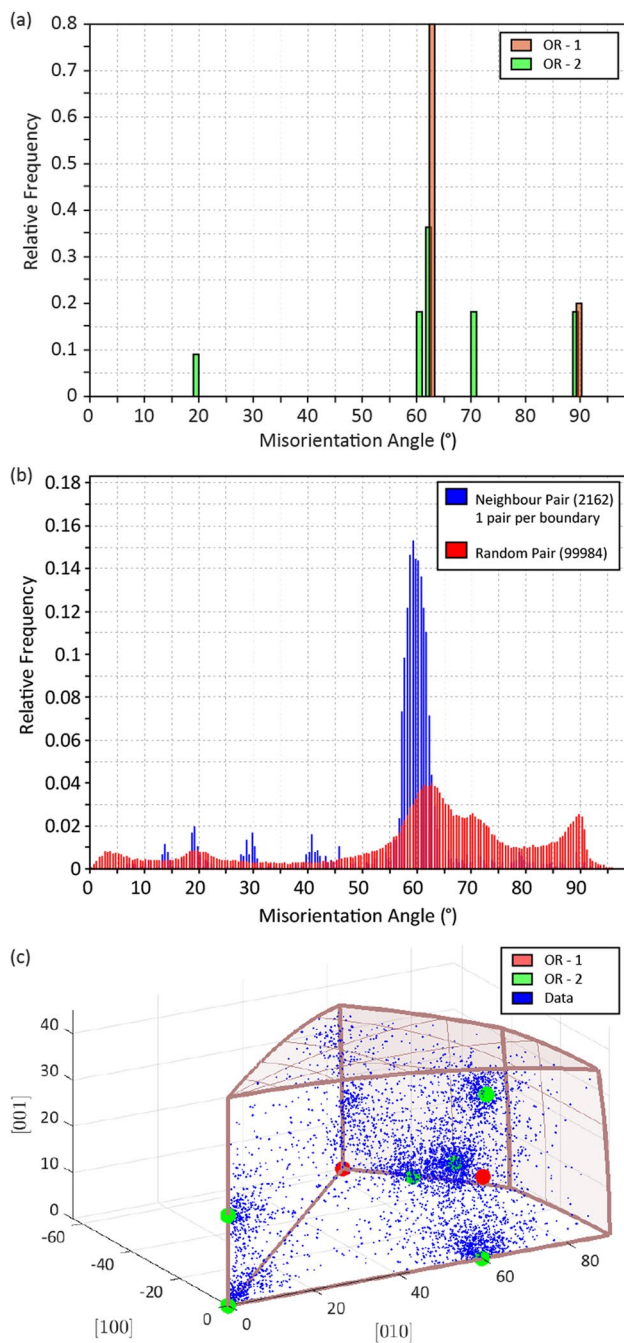


**Fig. 4** Misorientation distribution plots. **a** Simulations of expected misorientations distributions for the two posited orientation relationships between a cubic precursor and rutile. For clarity overlapping bars are shifted by half their width along the abscissa. **b** Experimental misorientation distribution histogram for the rutile in samples at one pair per boundary. **c** Misorientation space showing the modelled orientations (large dots) and the observed orientations (small dots) in misorientation angle-axis space

## Discussion

We have presented a range of datasets showing phase inheritance between titanium-bearing minerals during fluid-rock reactions in hydrothermal environments. We will now interpret the more complex relationships using well-constrained examples and explore the controlling factors in each case.

### Ilmenite breakdown to Rutile

The dataset from the Junction gold deposit (Fig. 1) depicts a simple system of an initial single crystal that is being replaced by two  $\text{TiO}_2$  polymorphs. Wenk et al. (2011) showed that ilmenite needles within plagioclase crystal are elongate in the  $[10\bar{1}0]$  direction and this is consistent with the orientation of the needle examine here (and from Plutonic Fig. 2). The rutile grains have a simple CPO where all three orientations of rutile have a common  $\langle 100 \rangle$  axis that aligns with the ilmenite  $c$ -axis. In each grain, the second symmetrically indistinguishable  $\langle 100 \rangle$  axis is aligned with the ilmenite  $a$ -axis. This results in a CPO that has the same symmetry elements (e.g. triad symmetry axis) as the original trigonal ilmenite needle. Previous studies of both iron oxidation and reduction during natural weathering and mineral processing of ilmenite, respectively, have identified the multiplicity in rutile orientations observed here. Detailed TEM studies of the replacement interfaces and interfaces between rutile grains have previously been used to identify two potential replacement relationships. Firstly,

$$[0001]_{\text{ilmenite}} // \langle 100 \rangle_{\text{rutile}} \text{ and } \langle 10\bar{1}0 \rangle_{\text{ilmenite}} // [001]_{\text{rutile}}$$

The relationship shown from the Junction datasets can be used to confirm the interpretation made from Fig. 5. Here, each of the two parts of the aggregate (subsets 1 and 2) shows the same CPO as the Junction dataset with the aligned  $\langle 100 \rangle$  axes being the triad symmetry axis. Moreover, the subset orientations are not independent but share a  $\langle 100 \rangle$  that is neither triad. This suggests that the original ilmenite grains that were replaced had related crystallography and shared  $a$ -axis.

Twinning in ilmenite has been documented as basal twins with twin plane (0001), and rhombohedral twins with both  $\{10\bar{1}1\}$  and  $\{10\bar{1}2\}$  as the twin planes. It is possible to reconstruct, using the relationships identified from the Junction rutile dataset, the orientation of the two ilmenite crystals that produced the rutile aggregates. The twins are not basal twins because if they were, then the two halves would share their basal plane and their  $c$ -axis orientations. The rhombohedral twinning is tractable but not intuitive and will be explored below.

The  $\{10\bar{1}1\}$  twin law is a composite twin, following the nomenclature of Christian and Mahajan (1995), where

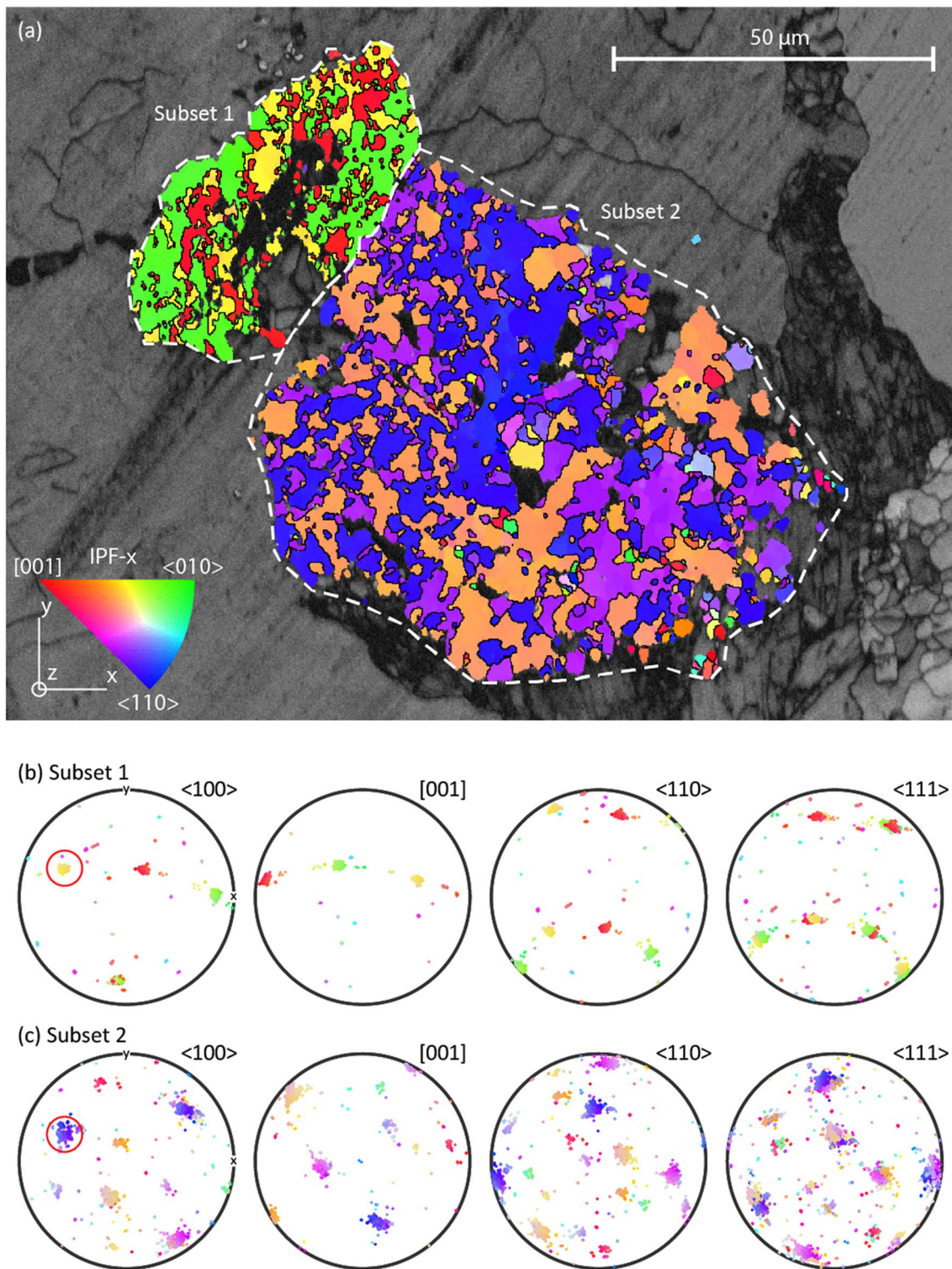


**Fig. 5** EBSD data of an anhedral rutile aggregate from Productora, Chile. **a** EBSD orientation map showing orientation variation within the aggregate. Two domains have been defined based on orientation differences and are highlighted using white dashed lines. **b** Pole figures coloured using the same colour scheme as for (a) showing the orientations of rutile within subset 1. **c** Pole figures coloured using the same colour scheme as for (a) showing the orientations of rutile within subset 2. For (b) and (c) the common  $\langle 100 \rangle$  direction is highlighted with a red circle

orientations of rutile within subset 1. **c** Pole figures coloured using the same colour scheme as for (a) showing the orientations of rutile within subset 2. For (b) and (c) the common  $\langle 100 \rangle$  direction is highlighted with a red circle



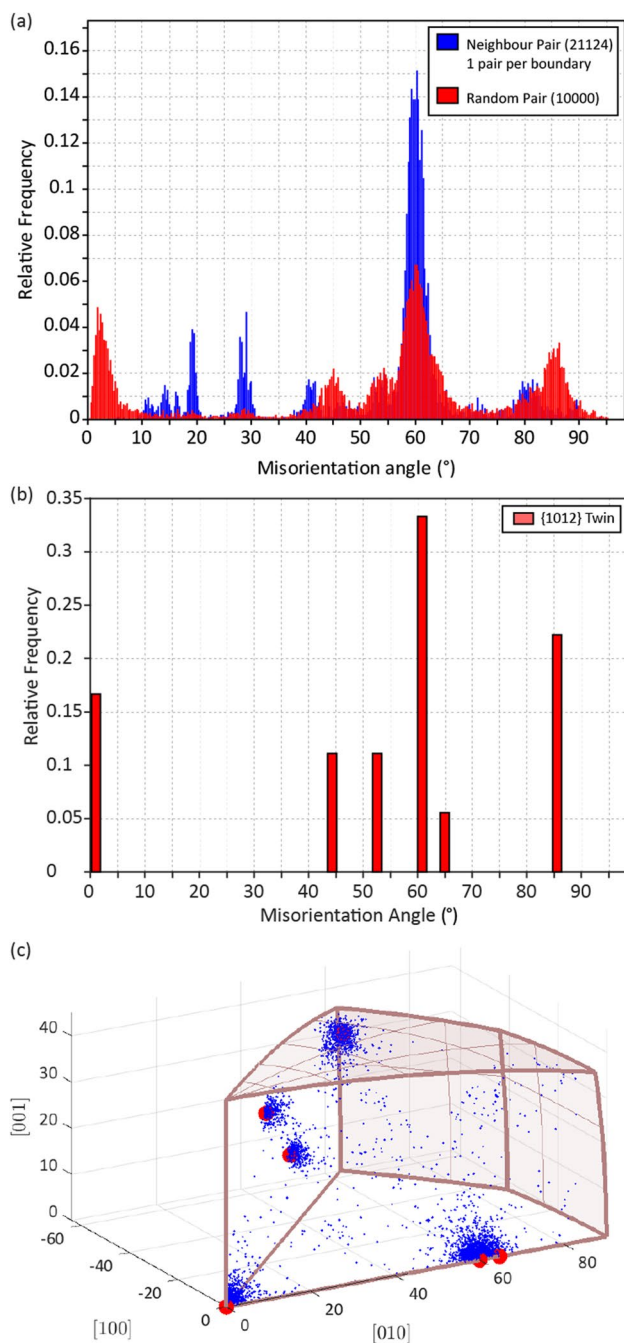


**Fig. 6** Misorientation distribution plots for the EBSD map shown in Fig. 5. **a** The blue graph shows misorientations from neighbouring pixels filtered to one pair of pixels per boundary segment and the red graph shows a selection of 10,000 misorientations between random pairs of pixels. Neighbour pairs show a strong peak at 60° highlighting the major twin relationship in rutile. Random pairs show a peak at 60° due to twinning and a subsidiary peak at 85° that results from the combination between the two subsets highlighted in Fig. 5. **b** Modelled misorientation angle distributions assuming that the rutile is replacing a twinned ilmenite grain with a {102} twin. Note the correspondence of peaks with major peaks in (a). **c** Misorientation space with the same hypothetical relationship as in (b) showing model (red dots) and data (blue dots) showing that there is correspondence between not only the angular distribution but also the misorientation axes

the twin plane, shear direction, conjugate plane and conjugate shear direction are all rational. The orientation relationship can be described by a 180° rotation around  $[\bar{1}012]$  (Wang et al. 1990) and results in coincidence of  $\{\bar{1}2\bar{1}0\}$  in the host and twin. The positive and negative zone axes are reversed by this rotation i.e.  $[\bar{1}2\bar{1}0] \rightarrow [1\bar{2}10]$  but because the planes are not polar, i.e.  $\{\bar{1}2\bar{1}0\} = \{1\bar{2}10\}$ , they are coincident. Moreover, following the transformation to rutile, it is not possible to recognise this polarity because none of the crystal directions are polar. This twin relationship also results in reorientation of the ilmenite c-axis by  $\sim 35^\circ$ .

The  $\{10\bar{1}2\}$  twin law has been observed in tectonically deformed Ontairo ilmenite (Minkin and Chao 1971) but has not been described in terms of rotation relationships. Assuming it is a composite twin similar to  $\{10\bar{1}1\}$ , twinning it would be also described by a 180° rotation around  $[\bar{1}011]$ . This orientation relationship also results in coincidence of  $\{\bar{1}2\bar{1}0\}$  between the host and the twin so that the two clusters of rutile grains will share one of their  $\langle 100 \rangle$  once the replacement occurs. The c-axis is reoriented by  $\sim 65^\circ$  by this rotation. Therefore, whilst the two laws are similar in their geometry, the angular relationship between the ilmenite c-axes, now the common  $[100]$  axes within each rutile subset, can help distinguish between the two. In addition, reconstructing the  $[\bar{1}011]$  and  $[\bar{1}012]$  orientation of the ilmenite should show that the rotation axis is shared between the two halves, and the twin plane trace should match that of the boundary for planar, coherent twinning.

The predicted misorientation relationships between the rutile grains can be modelled for the ilmenite grain containing  $\{10\bar{1}2\}$  twins (Fig. 6) in the same way as for the titanomagnetite to rutile transition. The observed misorientation angle distribution (Fig. 6a) for the neighbour pairs has a strong maximum at 60° because all the grains within each cluster are misoriented by 60° from each other. The random pair distribution gives information about relationships within and between each cluster. This also has a maximum at 60° but has subsidiary peaks at low angles,  $\sim 85^\circ$ , a shoulder on the 60° peak around 65° and two peaks at 45° and  $\sim 54^\circ$ . The modelled misorientation angle distribution (Fig. 6b) has peaks at the same values as the random pair angle distribution showing that the misorientation angles support the two clusters of rutile grains being derived from a single twinned ilmenite grain. Visualising the misorientation angles and axes using the 3D misorientation space for both the model and data together (Fig. 6c) shows a good correspondence not only for the angle distribution but also with the same axes as predicted from the model.

### Ilmenite replacement by other TiO<sub>2</sub> Polymorphs

The ilmenite needle from Junction is primarily replaced by anatase rather than rutile as might be expected from



thermodynamic calculations. Studies of nucleation that consider anisotropic surface energy have shown that it is possible to stabilise anatase given a proliferation of certain crystal faces and for very small grain sizes (Gribb and Banfield 1997). Once nucleated, these grains might persist as a metastable phase in the rock rather than reverting to rutile. The almost single crystal orientation of the anatase could be interpreted in two ways:

- (1) A strong and unique topotaxial relationship exists between the anatase and ilmenite meaning that multiple nuclei form in the same orientation separated by low-angle grain boundaries with small misorientation angles (e.g. Pearce et al. 2013).
- (2) Nucleation is much harder than growth meaning that only a small number of nuclei are successful and grow a single crystal

Here, we can use crystal symmetry arguments to suggest that (2) nucleation controls the microstructure. If multiple anatase nuclei occurred, the trigonal symmetry of ilmenite means that nucleation would be equally likely in three symmetrically equivalent orientations involving pairs of  $[0001]$  and  $\langle 01\bar{1}0 \rangle_{\text{ilmenite}}$ . Moreover, the anatase directions and planes involved have fourfold symmetry, each of which could nucleate on one of three ilmenite controlled orientations leading to a possible multiplicity of 12 different nuclei. This multiplicity was observed in zircon breakdown (Timms et al. 2017) and leads to apparently complex microstructures. Therefore, we suggest that case (2) is the more likely control where only one nucleus was successful. The spatial distribution of rutile grains adjacent to the edge of the ilmenite needle is a little more difficult to explain and might be related to extremely local variations in pH or other fluid compositional parameters where the conditions at the margins of the needle are buffered by the adjacent wall rock. However, further investigation of the controls on titania polymorph stability is required to resolve this.

### Polycrystal development during replacement

The Junction ilmenite needle single crystal is being replaced by a broadly single crystal orientation of titanite. There is a spread in orientations of titanite. This could be caused by deformation or could be caused by only a weak orientation relationship between the two phases. Weak orientation relationships result when there is a large mismatch in the crystal structures between the reactant and replacement phases and could be indicated, as in this case, by no obvious relationship between low order crystallographic planes or zone axes. Not only is there a spread in orientations within the titanite, but there is also a spread of orientations in the initial ilmenite. To test whether there really is a weak coupling between the

two phases or whether this results from deformation, we can investigate the microstructure in detail.

The titanite grains within the needle are polycrystalline with a mixture of high- and low-angle grain boundaries between them. The ilmenite needle also contains microstructures, such as variable orientation and low-angle boundaries, interpreted to arise from crystal plastic deformation. Both the ilmenite and titanite substructure could result from post-replacement deformation but the lack of sub-grains within the large titanite grains outside of the ilmenite needle means that this is unlikely. A more plausible explanation is that the ilmenite needle was deformed and then the replacement took place. The substructure in the finer-grained titanite is therefore inherited from the ilmenite because nucleation occurs controlled by multiple parts of the ilmenite lattice that are in different, but similar orientations leading to low-angle boundaries forming during static recrystallisation/replacement (Pearce et al. 2013; Spruzeniece et al. 2017). The case for multiple nuclei each with a slightly different orientation is further supported by the thin lamellae of ilmenite that still exist between the titanite grains. If this replacement was from a single (or a few) nucleus, then remnant ilmenite would be less likely to be preserved within the titanite.

### Epitaxial growth of Dolomite

The volume reduction associated with Fe removal during ilmenite breakdown leads to porosity being created. Whilst in many replacement reactions, this porosity is distributed through the replacing phase as micro- to nano-porosity, the porosity can also be concentrated at the reaction front (Pearce et al. 2013; Etschmann et al. 2014). Both ilmenite and dolomite are trigonal (space group R) minerals with similar atomic arrangements and comparable unit cell dimensions in the basal plane ( $a_{\text{ilm}} = 5.093 \text{ \AA}$  and  $a_{\text{dol}} = 4.842 \text{ \AA}$  differing by  $\sim 5\%$ ) although the  $c$ -axis lengths ( $c_{\text{ilm}} = 14.06 \text{ \AA}$  and  $c_{\text{dol}} = 15.95 \text{ \AA}$ ) differ by significantly more,  $\sim 13\%$ . Nucleation of dolomite within the porosity between ilmenite and anatase is controlled by the surface distribution of atoms in the ilmenite such that the dolomite–ilmenite interface has a similar atomic arrangement on both sides albeit with a dispersed orientation distribution due to mismatch between the two phases (Habler and Griffiths 2017). This expands the range of phases that can potentially be used to reconstruct altered mineralogy, relaxing the ‘common chemical component’ constraint between reactant and product.

### Unravelling destroyed phases

Phase heritage can be used to test numerous possible phase relationships and/or mineralogical precursors depending on the available constraints that remain in the rock (e.g. relict reactant phase present, independent knowledge

of replacement relationships). In the case of the twinned ilmenite from Productora, the ilmenite-to-rutile relationships have been established by previous studies (Stanković et al. 2016; Plavsá et al. 2018) and verified here (Fig. 1) and so we can infer the twin relationship based on studies of ilmenite and other corundum structured minerals (Minkin and Chao 1971; Wang et al. 1990). In the case of the rutile replacing the cubic mineral (Fig. 3), the obvious candidate for the precursor phase is titanomagnetite. Assuming that the original mineral had a composition similar to ulvospinel ( $X_{\text{ulv}}^{\text{mag}}$ ), we can use the EBSD data to investigate the amount of Ti gained or lost. The area of the triangular region now occupied by muscovite is 212400 pixels, using the molar volume of magnetite ( $Mv_{\text{mag}} = 45.534 \text{ cm}^3 \text{ mol}^{-1}$ ) and rutile ( $Mv_{\text{rut}} = 18.795 \text{ cm}^3 \text{ mol}^{-1}$ ), the predicted rutile volume ( $V_{\text{rut}}$ ) is:

$$V_{\text{rut}} = \frac{V_{\text{mag}}}{Mv_{\text{mag}}} X_{\text{ulv}}^{\text{mag}} Mv_{\text{rut}} = \frac{212400 \times 18.795}{45.534} = 87672 \text{ pixels} \quad (1)$$

The observed rutile volume is 74190 pixels, so using the Ti-rich endmember overestimates the amount of rutile that should be in the rock by ~18%. Rearranging Eq. 1 for the composition assuming Ti immobility at the scale of the microstructure gives the original composition as  $X_{\text{ulv}}^{\text{mag}} = 0.85$ . Whilst we cannot test the veracity of this compositional estimate, all available evidence suggests that the microstructure in Fig. 3 represents a relatively Ti-rich titanomagnetite that has been replaced by rutile.

## Conclusion

Titanium-bearing phases undergoing replacement reactions exhibit topotaxial relationships that can be used to infer the presence of now consumed phases. This may prove significant when assessing the redox state of magmas that generated igneous rocks that are now intensely altered, or when reviewing mineral chemistry data. Strong crystallographic relationships exist for ilmenite reacting to rutile (Junction case study) and have been inferred for titanomagnetite reacting to rutile (Productora euhedral case study) in line with previously observed relationships. Titanite forming during hydrothermal alteration (Plutonic case study) appears to show a crystallographic relationship to the reactant ilmenite although this is not straightforward, it appears reproducible because of the presence of a polycrystalline replacement phase. Anatase can form at the same time as rutile during ilmenite breakdown (Junction case study) and shows a possible relationship with the ilmenite although this is only present in a single grain, so further investigation is required to test how robust this observation is. Phases with few common components (e.g. oxygen) can undergo topotaxial

replacement suggesting that surface processes controlling nucleation may be an important and underestimated factor during metasomatism.

Electron backscatter diffraction data give large datasets of spatially constrained data that can be used to interrogate replacement microstructures. Given hypothetical orientation relationships, it is possible to model misorientation distributions within the replacement phase to test these relationships and discriminate between different options. Crystallographic preferred orientation symmetry can be used to construct hypothetical orientation relationships and deduce the symmetry of the reactant phase. Using a combination of misorientation angle distributions and 3d misorientation space analysis (Krakow et al. 2017) tests not only the axis and angle distributions but the relative frequency of predicted misorientations amongst product grains of completely consumed phases.

**Supplementary Information** The online version contains supplementary material available at <https://doi.org/10.1007/s00410-021-01775-8>.

**Acknowledgements** Part of this work was completed during the tenure of an CSIRO Office of the Chief Executive postdoctoral fellowship (MAP). Geoff Lloyd and an anonymous reviewer are thanked for their insightfully precise and constructive comments that have without doubt improved the manuscript. Nick Timms is thanked for stimulating discussions around twinning and for being instrumental in the development of ideas around phase heritage.

## References

- Agangi A, Reddy SM, Plavsá D et al (2019) Antimony in rutile as a pathfinder for orogenic gold deposits. *Ore Geol Rev* 106:1–11. <https://doi.org/10.1016/j.oregeorev.2019.01.018>
- Angel R, Milani S, Alvaro M, Nestola F (2015) OrientXplot: a program to analyse and display relative crystal orientations. *J Appl Crystallogr* 48:1330–1334. <https://doi.org/10.1107/S160057671501167X>
- Angiboust S, Harlov D (2017) Ilmenite breakdown and rutile-titanite stability in metagranitoids: natural observations and experimental results. *Am Mineral* 102:1696–1708. <https://doi.org/10.2138/am-2017-6064>
- Bachmann F, Hielscher R, Schaeben H (2010) Texture analysis with MTEX—free and open source software toolbox. *Solid State Phenom* 160:63–68
- Baier J, Audétat A, Keppler H (2008) The origin of the negative niobium tantalum anomaly in subduction zone magmas. *Earth Planet Sci Lett* 267:290–300. <https://doi.org/10.1016/j.epsl.2007.11.032>
- Barbosa PF, Lagoeiro L (2010) Crystallographic texture of the magnetite-hematite transformation: evidence for topotactic relationships in natural samples from Quadrilátero Ferrífero, Brazil. *Am Mineral* 95:118–125. <https://doi.org/10.2138/am.2010.3201>
- Bestmann M, Prior DJ (2003) Intragranular dynamic recrystallization in naturally deformed calcite marble: diffusion accommodated grain boundary sliding as a result of subgrain rotation recrystallization. *J Struct Geol* 25:1597–1613
- Bunge H-J (1982) Chapter 2—Orientation of Individual Crystallites. In: *Texture analysis in materials science*. Butterworth-Heinemann, pp 3–41

- Carey ML (1994) Petrography and geochemistry of selected sills from the Kambalda–Kalgoorlie region, WA. BSc Hons Thesis Aust Natl Univ Canberra Unpubl
- Cavosie AJ, Erickson TM, Timms NE (2015) Nanoscale records of ancient shock deformation: Reidite (ZrSiO<sub>4</sub>) in sandstone at the Ordovician Rock Elm impact crater. *Geology* 43:315–318. <https://doi.org/10.1130/G36489.1>
- Cavosie AJ, Timms NE, Erickson TM et al (2016) Transformations to granular zircon revealed: Twinning, reidite, and ZrO<sub>2</sub> in shocked zircon from Meteor Crater (Arizona, USA). *Geology* 44:703–706. <https://doi.org/10.1130/G38043.1>
- Cayron C (2007) ARPGE: a computer program to automatically reconstruct the parent grains from electron backscatter diffraction data. *J Appl Crystallogr* 40:1183–1188. <https://doi.org/10.1107/S0021889807048777>
- Cayron C, Douillard T, Sibila A et al (2010) Reconstruction of the cubic and tetragonal parent grains from electron backscatter diffraction maps of monoclinic zirconia. *J Am Ceram Soc* 93:2541–2544. <https://doi.org/10.1111/j.1551-2916.2010.03894.x>
- Cho J-H, Rollett AD, Oh KH (2005) Determination of a mean orientation in electron backscatter diffraction measurements. *Metall Mater Trans A* 36:3427–3438. <https://doi.org/10.1007/s11661-005-0016-4>
- Christian JW, Mahajan S (1995) Deformation twinning. *Prog Mater Sci* 39:1–157. [https://doi.org/10.1016/0079-6425\(94\)00007-7](https://doi.org/10.1016/0079-6425(94)00007-7)
- Crameri F (2018) Scientific colour-maps. Zenodo. <https://doi.org/10.5281/zenodo.1243862>
- Crameri F, Shephard GE, Heron PJ (2020) The misuse of colour in science communication. *Nat Commun* 11:1–10. <https://doi.org/10.1038/s41467-020-19160-7>
- Diener JFA, Powell R (2012) Revised activity–composition models for clinopyroxene and amphibole. *J Metamorph Geol* 30:131–142. <https://doi.org/10.1111/j.1525-1314.2011.00959.x>
- Erickson TM, Timms NE, Pearce MA et al (2019) Shock-produced high-pressure (La, Ce, Th) PO<sub>4</sub> polymorph revealed by microstructural phase heritage of monazite. *Geology* 47:504–508
- Escolme A (2017) Geology, geochemistry and geometallurgy of the Productora Cu–Au–Mo deposit, Chile. PhD Thesis, University of Tasmania
- Escolme A, Cooke DR, Hunt J et al (2020) The Productora Cu–Au–Mo deposit, Chile: a mesozoic magmatic–hydrothermal breccia complex with both porphyry and iron oxide Cu–Au affinities. *Econ Geol* 115:543–580. <https://doi.org/10.5382/econgeo.4718>
- Etschmann B, Brugger J, Pearce MA et al (2014) Grain boundaries as microreactors during reactive fluid flow: experimental dolomitization of a calcite marble. *Contrib Mineral Petrol* 168:1–12. <https://doi.org/10.1007/s00410-014-1045-z>
- Gazley MF, Vry JK, Boorman JC (2011) P–T Evolution in Greenstone-Belt Mafic Amphibolites; an Example from Plutonic Gold Mine, Marymia Inlier, Western Australia. *J Metamorph Geol* 29:685–697. <https://doi.org/10.1111/j.1525-1314.2011.00936.x>
- Gazley M, Vry J, Pearce M (2014) Further evidence for ~8 kbar amphibolite facies metamorphism in the Marymia Inlier, Western Australia. *Aust J Earth Sci* 61:919–926
- Goresy AE, Dubrovinsky L, Gillet P et al (2010) Akaogiite: an ultradense polymorph of TiO<sub>2</sub> with the baddeleyite-type structure, in shocked garnet gneiss from the Ries Crater, Germany. *Am Mineral* 95:892–895. <https://doi.org/10.2138/am.2010.3425>
- Gribb AA, Banfield JF (1997) Particle size effects on transformation kinetics and phase stability in nanocrystalline TiO<sub>2</sub>. *Am Mineral* 82:717–728
- Habler G, Griffiths T (2017) Crystallographic orientation relationships. In: Heinrich W, Abart R (eds) Mineral reaction kinetics: Microstructures, textures, chemical and isotopic signatures. Mineralogical Society of Great Britain and Ireland, pp 541–585. <https://doi.org/10.1180/EMU-notes.16.15>
- Hackenberg RE (2012) The historical development of phase transformations understanding in ferrous alloys. *Phase Transformations in Steels*. Woodhead Publishing, Elsevier, pp 3–55
- Halfpenny A, Prior DJ, Wheeler J (2006) Analysis of dynamic recrystallization and nucleation in a quartzite mylonite. *Tectonophysics* 427:3–14
- Humbert M, Gey N, Muller J, Esling C (1996) Determination of a mean orientation from a cloud of orientations. Application to electron back-scattering pattern measurements. *J Appl Crystallogr* 29:662–666
- Hwang S-L, Shen P, Chu H-T, Yui T-F (2000) Nanometer-size α-PbO<sub>2</sub>-type TiO<sub>2</sub> in garnet: a thermobarometer for ultrahigh-pressure metamorphism. *Science* 288:321–324. <https://doi.org/10.1126/science.288.5464.321>
- Kasioptas A, Perdikouri C, Putnis CV, Putnis A (2008) Pseudomorphic replacement of single calcium carbonate crystals by polycrystalline apatite. *Mineral Mag* 72:77–80. <https://doi.org/10.1180/minmag.2008.072.1.77>
- Kasioptas A, Geisler T, Perdikouri C et al (2011) Polycrystalline apatite synthesized by hydrothermal replacement of calcium carbonates. *Geochim Cosmochim Acta* 75:3486–3500. <https://doi.org/10.1016/j.gca.2011.03.027>
- Korzhinskii DS (1965) The theory of systems with perfectly mobile components and processes of mineral formation. *Am J Sci* 263:193–205. <https://doi.org/10.2475/ajs.263.3.193>
- Krakow R, Bennett RJ, Johnstone DN et al (2017) On three-dimensional misorientation spaces. *Proc R Soc Math Phys Eng Sci* 473:20170274
- Leroux H, Reimold WU, Koeberl C et al (1999) Experimental shock deformation in zircon: a transmission electron microscopic study. *Earth Planet Sci Lett* 169:291–301. [https://doi.org/10.1016/S0012-821X\(99\)00082-5](https://doi.org/10.1016/S0012-821X(99)00082-5)
- Lindgren W (1912) The nature of replacement. *Econ Geol* 7:521–535. <https://doi.org/10.2113/gsecongeo.7.6.521>
- Lloyd GE, Farmer AB, Mainprice D (1997) Misorientation analysis and the formation and orientation of subgrain and grain boundaries. *Tectonophysics* 279:55–78
- Mackenzie JK, Thomson MJ (1957) Some statistics associated with the random disorientation of cubes. *Biometrika* 44:205–210. <https://doi.org/10.1093/biomet/44.1-2.205>
- MacLean WH, Kranidiotis P (1987) Immobile elements as monitors of mass transfer in hydrothermal alteration; Phelps Dodge massive sulfide deposit, Matagami, Quebec. *Econ Geol* 82:951–962. <https://doi.org/10.2113/gsecongeo.82.4.951>
- Mainprice D, Lloyd GE, Casey M (1993) Individual orientation measurements in quartz polycrystals—advantages and limitations for texture and petrophysical property determinations. *J Struct Geol* 15:1169–1187
- McNamara DD, Wheeler J, Pearce M, Prior DJ (2012) Fabrics produced mimetically during static metamorphism in retrogressed eclogites from the Zermatt-Saas zone, Western Italian Alps. *J Struct Geol* 44:167–178
- Minkin JA, Chao ECT (1971) Single crystal X-ray investigation of deformation in terrestrial and lunar ilmenite. *Lunar Planet Sci Conf Proc* 2:237
- Pearce MA (2015a) EBSDinterp v1.0. CSIRO Data Collection. <https://doi.org/10.4225/08/5510090C6E620>
- Pearce MA (2015b) EBSDinterp 1.0: a MATLAB® program to perform microstructurally constrained interpolation of EBSD data. *Microsc Microanal* 21:985–993. <https://doi.org/10.1017/S1431927615000781>
- Pearce MA (2020) EBSD data documenting replacement reactions in Ti-bearing Minerals. CSIRO Data Collection v1. <https://doi.org/10.25919/490k-ba64>
- Pearce MA, Timms NE, Hough RM, Cleverley JS (2013) Reaction mechanism for the replacement of calcite by dolomite and



- siderite: implications for geochemistry, microstructure and porosity evolution during hydrothermal mineralisation. *Contrib Mineral Petrol* 166:995–1009. <https://doi.org/10.1007/s00410-013-0905-2>
- Pearce MA, White AJR, Fisher LA et al (2015) Gold deposition caused by carbonation of biotite during late-stage fluid flow. *Lithos* 239:114–127. <https://doi.org/10.1016/j.lithos.2015.10.010>
- Plavska D, Reddy SM, Agangi A et al (2018) Microstructural, trace element and geochronological characterization of TiO<sub>2</sub> polymorphs and implications for mineral exploration. *Chem Geol* 476:130–149. <https://doi.org/10.1016/j.chemgeo.2017.11.011>
- Polito PA, Bone Y, Clarke JDA, Mernagh TP (2001) Compositional zoning of fluid inclusions in the Archaean Junction gold deposit, Western Australia: a process of fluid–wall-rock interaction? *Aust J Earth Sci* 48:833–855. <https://doi.org/10.1046/j.1440-0952.2001.00903.x>
- Pollok K, Putnis CV, Putnis A (2011) Mineral replacement reactions in solid solution–aqueous solution systems: volume changes, reactions paths and end-points using the example of model salt systems. *Am J Sci* 311:211–236. <https://doi.org/10.2475/03.2011.02>
- Pospiech J, Sztwiertnia K, Haessner F (1986) The Misorientation Distribution Function. In: *Textures Microstruct*. <https://www.hindawi.com/journals/tsm/1986/575690/>. Accessed 11 Jan 2021
- Prior DJ, Boyle AP, Brenker F et al (1999) The application of electron backscatter diffraction and orientation contrast imaging in the SEM to textural problems in rocks. *Am Mineral* 84:1741–1759
- Prior DJ, Wheeler J, Peruzzo L et al (2002) Some garnet micro structures: an illustration of the potential of orientation maps and misorientation analysis in microstructural studies. *J Struct Geol* 24:999–1011
- Prior DJ, Mariani E, Wheeler J (2009) EBSD in the Earth Sciences: applications, common practice and challenges. In: Schwatz AJ, Kumar M, Adams BL, Field DP (eds) *Electron backscatter diffraction in materials science*. Springer, New York
- Putnis A (2009) Mineral replacement reactions. *Rev Mineral Geochem* 70:87–124. <https://doi.org/10.2138/rmg.2009.70.3>
- Qian G, Brugger J, Skinner WM et al (2010) An experimental study of the mechanism of the replacement of magnetite by pyrite up to 300 degrees C. *Geochim Cosmochim Acta* 74:5610–5630. <https://doi.org/10.1016/j.gca.2010.06.035>
- Rečnik A, Stanković N, Daneu N (2015) Topotaxial reactions during the genesis of oriented rutile/hematite intergrowths from Mwini-lunga (Zambia). *Contrib Mineral Petrol* 169:1–22. <https://doi.org/10.1007/s00410-015-1107-x>
- Ryerson FJ, Watson EB (1987) Rutile saturation in magmas: implications for TiNbTa depletion in island-arc basalts. *Earth Planet Sci Lett* 86:225–239
- Schaeben H (1997) A simple standard orientation density function: the hyperspherical de la vallée poussin kernel. *Phys Status Solidi B* 200:367–376. [https://doi.org/10.1002/1521-3951\(199704\)200:2%3c367::AID-PSSB367%3e3.0.CO;2-I](https://doi.org/10.1002/1521-3951(199704)200:2%3c367::AID-PSSB367%3e3.0.CO;2-I)
- Schouten C (1946) Some notes on micro-pseudomorphism. *Econ Geol* 41:348–382. <https://doi.org/10.2113/gsecongeo.41.4.348>
- Scott KM, Radford NW, Hough RM, Reddy SM (2011) Rutile compositions in the Kalgoorlie Goldfields and their implications for exploration. *Aust J Earth Sci* 58:803–812. <https://doi.org/10.1080/08120099.2011.600334>
- Spruzeniece L, Piazzolo S, Maynard-Casely HE (2017) Deformation-resembling microstructure created by fluid-mediated dissolution–precipitation reactions. *Nat Commun* 8:14032. <https://doi.org/10.1038/ncomms14032>
- Stanković N, Rečnik A, Daneu N (2016) Topotaxial reactions during oxidation of ilmenite single crystal. *J Mater Sci* 51:958–968. <https://doi.org/10.1007/s10853-015-9425-y>
- Timms NE, Erickson TM, Zanetti MR et al (2017) Cubic zirconia in > 2370 °C impact melt records Earth’s hottest crust. *Earth Planet Sci Lett* 477:52–58
- Triebold S, Luvizotto GL, Tolosana-Delgado R et al (2011) Discrimination of TiO<sub>2</sub> polymorphs in sedimentary and metamorphic rocks. *Contrib Mineral Petrol* 161:581–596. <https://doi.org/10.1007/s00410-010-0551-x>
- Van Baalen MR (1993) Titanium mobility in metamorphic systems: a review. *Chem Geol* 110:233–249. [https://doi.org/10.1016/0009-2541\(93\)90256-I](https://doi.org/10.1016/0009-2541(93)90256-I)
- Vernooij MGC, Kunze K, den Brok B (2006) “Brittle” shear zones in experimentally deformed quartz single crystals. *J Struct Geol* 28:1292–1306
- Wang YG, Ye HQ, Kuo KH, Ximen L (1990) A HREM study of non-basal twinning and superlattices in ilmenite. *J Appl Crystallogr* 23:82–87
- Wenk H-R, Chen K, Smith R (2011) Morphology and microstructure of magnetite and ilmenite inclusions in plagioclase from Adirondack anorthositic gneiss. *Am Mineral* 96:1316–1324. <https://doi.org/10.2138/am.2011.3760>
- Wheeler J, Prior DJ, Jiang Z et al (2001) The petrological significance of misorientations between grains. *Contrib Mineral Petrol* 141:109–124
- Xia F, Brugger J, Chen G et al (2009) Mechanism and kinetics of pseudomorphic mineral replacement reactions: a case study of the replacement of pentlandite by violarite. *Geochim Cosmochim Acta* 73:1945–1969. <https://doi.org/10.1016/j.gca.2009.01.007>
- Xia F, Brugger J, Ngothai Y et al (2009) Three-dimensional ordered arrays of zeolite nanocrystals with uniform size and orientation by a pseudomorphic coupled dissolution–reprecipitation replacement route. *Cryst Growth Des* 9:4902–4906. <https://doi.org/10.1021/cg900691a>

**Publisher’s Note** Springer Nature remains neutral with regard to jurisdictional claims in published maps and institutional affiliations.

## Authors and Affiliations

Mark Pearce<sup>1</sup>  · Angela Escolme<sup>2</sup>

<sup>1</sup> CSIRO Mineral Resources, Australian Resources Research Centre, 26 Dick Perry Avenue, Kensington, WA 6151, Australia

<sup>2</sup> Centre for Ore Deposits and Earth Sciences (CODES), University of Tasmania, Hobart, TAS 7001, Australia